



HEAT FLOW DISTRIBUTION CHARACTERISTICS OF SOLID WALL OF NOZZLE FLOWMETER

L.H. Tong^a, Y.L. Zhang^{b,†}, T.H. Yu^a, B.Y. Luo^c, J.F. Li^b

^a Quzhou Academy of Metrology and Quality Inspection, Quzhou, Zhejiang, 324024, China

^b College of Mechanical Engineering, Quzhou University, Quzhou, Zhejiang, 324000, China

^c Zhejiang University, Hangzhou, Zhejiang, 310000, China

ABSTRACT

In order to explore the thermal characteristics of a small nozzle flowmeter in the solid domain when transporting medium with different temperatures, the steady and transient thermal characteristics of each component of the nozzle flowmeter are calculated based on the finite element method. Results showed that the numerical calculation method could effectively reveal the internal thermal characteristics. When transporting high temperature medium, there was an obvious temperature stratification near the inner wall; when the inner wall temperature rose from 50 °C to 700 °C, the heat flow field at the inlet and outlet of the flowmeter increased significantly with the increase of temperature.

Keywords: *Nozzle flowmeter; Numerical calculation; Neat flow; Temperature*

1. INTRODUCTION

In modern industry, flow, pressure and temperature field are known as the three major industrial detection parameters. As the most important instrument for fluid flow detection, flowmeter is more and more widely used in modern industry, such as, orifice flowmeter, ultrasonic flowmeter, differential pressure orifice flowmeter, vortex flowmeter, etc. Kolodzie et al. experimentally studied the influence of structural parameters such as hole diameter, plate thickness and hole pitch on the discharge coefficients through orifice plate flowmeter, and established the relationship between structural parameters and discharge coefficients (Kolodzie Jr and Van Winkle (1957)). Smith et al. corrected Kolodzie 's formula of orifice plate discharge coefficients by data analysis and experiments (Smith Jr and Van Winkle (1958)). Numachi et al. studied the effect of cavitation on the discharge coefficient for orifice plate flowmeter and pointed out that the critical cavitation number for orifice flowmeter (Numachi et al. (1960)). DeOtt et al. measured the axial velocity distribution, Reynolds stress tensor, static wall pressure, and wall shear stress of the center line of the orifice plate (DeOtte et al. (1991)). Morrison et al. discovered recirculation zones in both upstream and downstream of the orifice plate, and pointed out that the fluid separated from the orifice plate at the throat and reattached to the pipe wall at 5.3 times the radius downstream away from the orifice plate (Morrison et al. (1993)). Kim et al. took into account the influences of the diameter ratio and thickness of the orifice plate, and experimentally studied the changing rules of the discharge coefficient of orifice plate under different cavitation numbers (Kim et al. (1998)). Huang et al. experimentally tested the discharge coefficient of the perforated orifice with different thicknesses, porosities and hole distributions, and compared with the standard orifice plate. Results showed that the perforated orifice flowmeter had the advantages of larger discharge coefficient, lower critical Reynolds number and a more stable flow field than the standard orifice plate (Huang et al. (2013)).

Schena et al. found that temperature would affect the output signal of orifice flowmeter sensor through experiments, and proposed a correction method based on theoretical analysis (Schena et al. (2013)). He et al. applied the numerical method to simulate flow field in a 50mm-diameter swirlmeter, and proposed an improved swirlmeter with inlet guide vanes which could effectively reduce the pressure loss (He et al. (2008)). Fu et al. studied the characteristics of the internal flow field of the swirlmeter by computational fluid dynamics (CFD) method, and proposed a method of signal differential processing to improve the anti-interference ability of the swirlmeter (Fu and Yang (2001), Peng et al. (2004)). Li et al. designed a new type of swirlmeter by numerical simulation, and analysed the influence of different parameters on the swirlmeter (Li et al. (2012)). Jin et al. added a venturi tube after the spinner to detect the weak fluid signals by accelerating the fluid (Jin (2014)). Ma et al. experimentally proved that using a new sensor installation method and differential processing method could eliminate the influence of pipe vibration on swirlmeter (Ma and Zhao (2014)). Sahand et al. designed a new multiphase flowmeter by coupling a slotted orifice plate with a swirl flowmeter, and evaluated the performance with high-accuracy two-phase flow measurements (Sahand et al. (2014)). In addition, other all kinds of flow characteristics has also been deeply studied (Cheng et al. (2020), Zhang et al. (2019), Chen et al. (2016), Cui et al. (2015), Bilicki et al. (2002), Kock and Herwig et al. (2004), Tao et al. (2020), Cui et al. (2020), Cheng et al. (2022), Cheng and Zhang et al. (2022), Jia et al. (2022), Jia et al. (2022), Jia et al. (2023)).

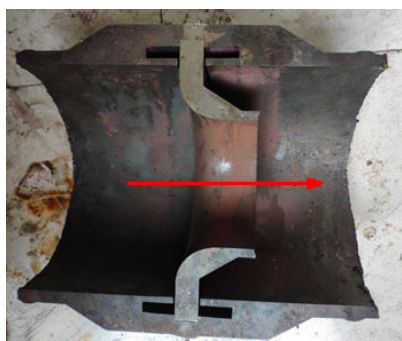
It could be concluded that the current research on nozzle flowmeter is still very limited. The internal flow characteristics and metering characteristics are not involved. The internal structural characteristics in the case of high temperature are also not revealed yet. The purpose of this study is to explore the nozzle flowmeter thermal characteristics at different temperatures by the numerical simulation under different conditions.

[†] Corresponding author. Email: zhang002@sina.com

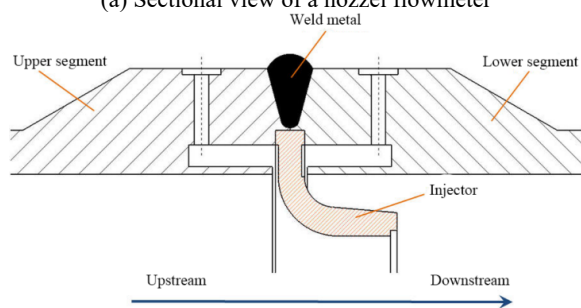
2. NUMERICAL MODEL AND CALCULATION METHOD

2.1 Flowmeter geometry

The structure and sectional view of the nozzle flowmeter are shown in Fig. 1. The flowmeter is mainly composed of the front measuring tube, the rear measuring tube, the nozzle and the weld metal. The inlet diameter of the measuring tube is 213 mm. The overall diameter of the measuring tube is 358mm. The outlet diameter of the measuring tube is 223 mm. There are several upstream and downstream pressure ports with a diameter of 27 mm on the periphery of the measuring tube. The material of measuring tube is 12CrMoVG.



(a) Sectional view of a nozzle flowmeter



(b) Structure diagram

Fig. 1 Overall structure diagram

2.2 3D modeling and meshing

The finite element analysis software ANSYS Workbench was applied to numerically simulate the thermal field of nozzle flowmeter. The three-dimensional modelling software UG was used to model the solid structure of the nozzle flowmeter in equal proportion, and the solid models of the front measuring tube, the rear measuring tube, the eight-slot nozzle and the weld metal were obtained. Fig. 2 displays the calculation domain of the nozzle flowmeter solid structure.

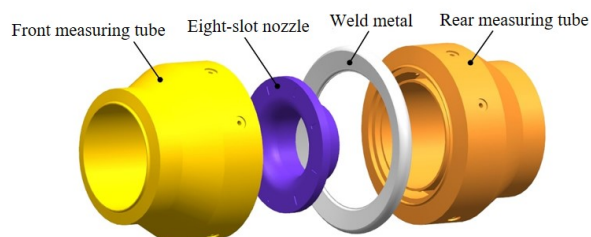


Fig. 2 3D model of nozzle flowmeter

In this study, ICEM software is used to mesh the solid domain of nozzle flowmeter. The unstructured tetrahedral grids were adopted to solve the complex computational domains such as the front measuring tube, the rear measuring tube, the eight-slot nozzle and the weld metal for good adaptability. The hexahedral core is used inside. The grid independence study is also carried out for present model, it is found that the calculating error is less than 1% and there is almost no difference among the solid fields. Consequently, the influence of the grid numbers

on the numerical results can be ignored. The number of grids of the front measuring tube, the rear measuring tube, the eight-groove nozzle and the weld metal are 63875, 63872, 1424041 and 38623, respectively, and the grid number is 1590411 in total.

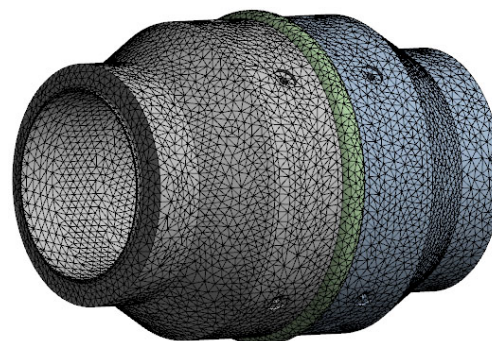


Fig. 3 Grid diagram

2.3 Thermodynamic model

The heat transfer modes include heat conduction, heat convection and heat radiation. The current work mainly applied the heat conduction model to solve the thermodynamic problems.

$$q = -\lambda \text{grad}t = -\lambda \frac{\partial t}{\partial n} n \quad (1)$$

where q is heat flux density, $J/(m^2 \cdot s)$; λ is thermal conductivity, $W/(m \cdot K)$; $\text{grad}t$ is the temperature gradient of a point in the medium; $\frac{\partial t}{\partial n}$ is the changing rate of temperature in the normal direction of the isothermal surface at this point; n is the unit vector in the normal direction of the isotherm through this point.

3. RESULTS AND DISCUSSION

The thermal effect of nozzle flowmeter with different inner wall temperatures was simulated by ANSYS software. The numerical calculation of the steady-state thermal effect of the nozzle flowmeter solid structure was carried out at the inner wall temperature of 50 °C, 100 °C, 300 °C, 500 °C and 700 °C. The temperature on outside surface of nozzle flowmeter is constant, namely that it is always 20 °C. The temperature and heat flow distributions of the nozzle flowmeter with different inner wall temperatures were compared and analyzed.

3.1 Monitoring path

Fig. 4 displays the schematic diagrams of the monitoring paths of the upstream and downstream pressure taps of nozzle.

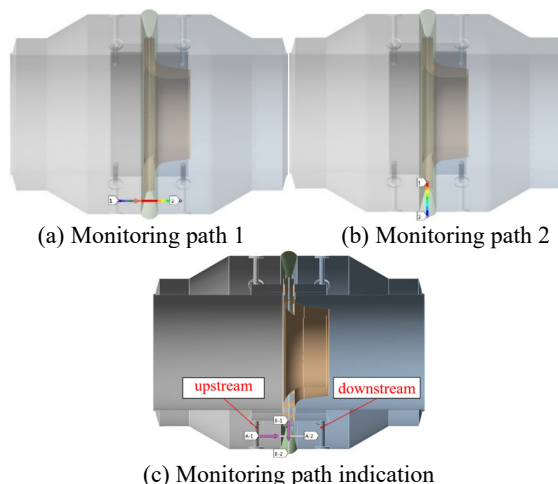


Fig. 4 Schematic diagrams of detection path for nozzle upstream and downstream intake

In Fig. 4 (c), it can be seen that the monitoring path 1 is the path from the upstream pressure tapping point A1 to the downstream pressure tapping point A2, parallel to the gas flow direction. Monitoring path 2 is the path from B1 near the inner wall to B2 on the outer wall, perpendicular to the gas flow direction. The effects of different inner wall temperatures on the distributions of temperature and heat flow on paths 1 and 2 were obtained by monitoring paths 1 and 2, respectively.

3.2 Steady state heat flow analysis

Fig. 5 shows the heat flow distribution of monitoring path 1 under different inner wall temperatures. The total heat flow increased first, then decreased and then increased again on the path from the upstream pressure tapping point to the downstream pressure tapping point in all the cases. The peak value appeared at 0.42 L and 0.58 L, and the valley value appeared at 0.5 L. When the inner wall temperature was 50 °C, 100 °C, 300 °C, 500 °C and 700 °C, the maximum peak values of heat flow on monitoring path 1 were 0.037 W/mm², 0.099 W/mm², 0.35 W/mm², 0.60 W/mm² and 0.85 W/mm², respectively, indicating that as the inner wall temperature of the nozzle flowmeter increased, the heat flow peak value of the monitoring path 1 also increased. When the inner wall temperature of the nozzle flowmeter was 50 °C, 100 °C, 300 °C, 500 °C and 700 °C, the total heat flow values at 0.5L of the monitoring path 1 were 0.035 W/mm², 0.094 W/mm², 0.329 W/mm², 0.565 W/mm² and 0.801 W/mm², respectively. When the inner wall temperature of nozzle flowmeter is 50 °C, 100 °C, 300 °C, 500 °C and 700 °C, the maximum amplitudes (maximum peak - minimum valley) of monitoring path 1 were 0.002 W/mm², 0.007 W/mm², 0.03 W/mm², 0.05 W/mm² and 0.07 W/mm², respectively. The above results showed that as the inner wall temperature of the nozzle flowmeter increased, the maximum amplitude of the total heat flow on the monitoring path 1 also increased.

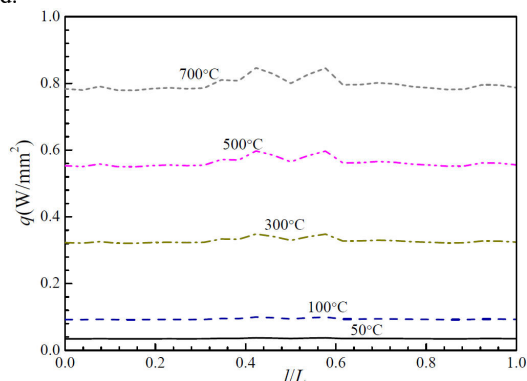


Fig. 5 Heat flow distribution of monitoring path 1 under different inner wall temperatures

Fig. 6 shows the total heat flow distribution of monitoring path 2 under different inner wall temperatures.

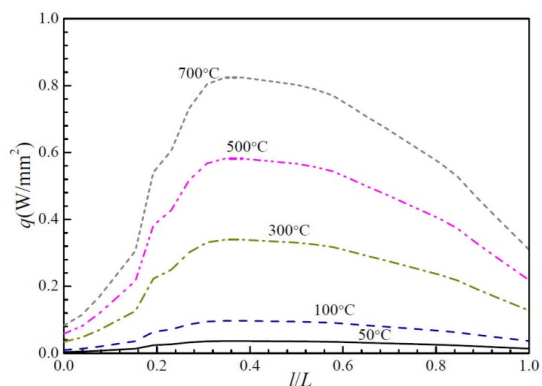


Fig. 6 Heat flow distribution of monitoring path 2 under different inner wall temperatures

The total heat flow increased first and then decreased on the path from the inner wall to the outer wall in all the cases, and reached the

peak at 0.35 L. When the inner wall temperature of the nozzle flowmeter was 50 °C, 100 °C, 300 °C, 500 °C and 700 °C, the maximum peak values of the total heat flow on the monitoring path 2 were 0.036 W/mm², 0.097 W/mm², 0.339 W/mm², 0.582 W/mm² and 0.824 W/mm², respectively. It showed that the total heat flow peak value of the monitoring path 2 increased as the inner wall temperature of the nozzle flowmeter increased. When the inner wall temperature of nozzle flowmeter was 50 °C, 100 °C, 300 °C, 500 °C and 700 °C, the maximum amplitudes (maximum peak - minimum valley) of monitoring path 2 were 0.03285 W/mm², 0.087 W/mm², 0.305 W/mm², 0.524 W/mm² and 0.741 W/mm², respectively.

Fig. 7 shows the heat flow distribution of monitoring path 1 in X direction under different inner wall temperatures. The total heat flow decreased first, then increased and then decreased again on the path in X direction from the upstream pressure tapping point to the downstream pressure tapping point in all the cases. The valley value and peak value appeared at 0.35 L and 0.73 L, respectively. When the inner wall temperature of nozzle flowmeter was 50 °C, 100 °C, 300 °C, 500 °C and 700 °C, the maximum peak values of monitoring path 1 were 0.00305 W/mm², 0.00812 W/mm², 0.0284 W/mm², 0.0487 W/mm² and 0.069 W/mm², respectively. It showed that as the inner wall temperature of the nozzle flowmeter increased, the X-direction heat flow peak value of the monitoring path 1 also increased. When the inner wall temperature of the nozzle flowmeter was 50 °C, 100 °C, 300 °C, 500 °C and 700 °C, the minimum valley values of the monitoring path 1 were -0.00304 W/mm², -0.0081 W/mm², -0.0284 W/mm², -0.0487 W/mm² and -0.0690 W/mm², respectively. When the inner wall temperature of nozzle flowmeter was 50 °C, 100 °C, 300 °C, 500 °C and 700 °C, the maximum amplitudes (maximum peak - minimum valley) of monitoring path 1 is 0.00609 W/mm², 0.0365 W/mm², 0.0771 W/mm², 0.0974 W/mm² and 0.138 W/mm², respectively. It could be concluded that as the inner wall temperature of the nozzle flowmeter increased, the maximum amplitude of the X-direction heat flow on the monitoring path 1 also increased.

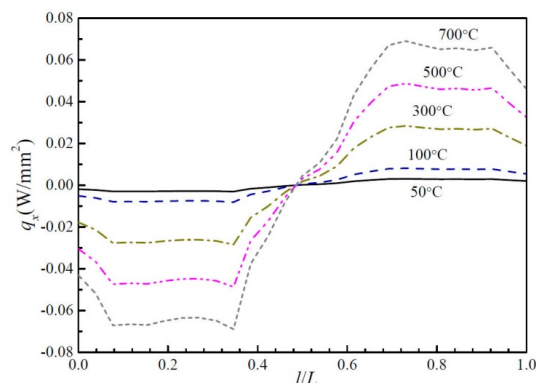


Fig. 7 Heat flow distribution of monitoring path 1 in X direction under different inner wall temperatures

Fig. 8 shows the heat flow distribution of monitoring path 2 in X direction under different inner wall temperatures. In all cases, the heat flow in the X direction along the path from the inner wall to the outer wall first decreased, then increased and finally decreased. The valley and peak were reached at 0.19 L and 0.27 L, respectively. When the inner wall temperature of the nozzle flowmeter was 50 °C, 100 °C, 300 °C, 500 °C and 700 °C, the maximum peak values of the X-direction heat flow on the monitoring path 2 were 0.0028 W/mm², 0.0075 W/mm², 0.0261 W/mm², 0.0448 W/mm² and 0.0635 W/mm², respectively. It showed that as the inner wall temperature of the nozzle flowmeter increased, the X-direction heat flow peak of the monitoring path 2 also increased. When the inner wall temperature of the nozzle flowmeter was 50 °C, 100 °C, 300 °C, 500 °C and 700 °C, the minimum valley values of the X-direction heat flow on the monitoring path 2 were -0.0038 W/mm², -0.010 W/mm², -0.0357 W/mm², -0.061 W/mm² and -0.0866 W/mm², respectively. When the inner wall

temperature of the nozzle flowmeter was 50 °C, 100 °C, 300 °C, 500 °C and 700 °C, the maximum amplitudes (maximum peak - minimum valley) of the monitoring path 2 were 0.0066 W/mm², 0.0775 W/mm², 0.0618 W/mm², 0.1058 W/mm² and 0.1501 W/mm², respectively. It showed that the maximum amplitude of the monitoring path 2 increased as the inner wall temperature of the nozzle flowmeter increased.

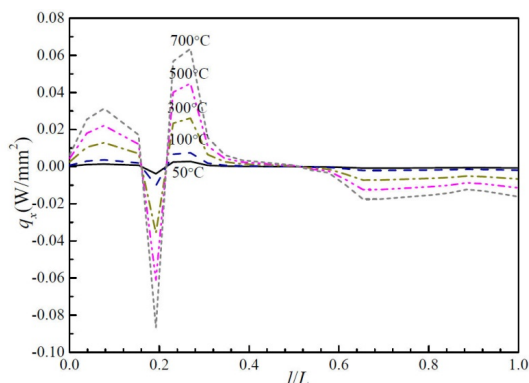


Fig. 8 Heat flow distribution of monitoring path 2 in X direction under different inner wall temperatures

Fig. 9 shows the heat flow distribution of monitoring path 1 in Y direction at different inner wall temperatures. In all cases, there were multiple peaks and valleys in the Y-direction heat flow distribution on the path from the upstream pressure tapping point to the downstream pressure tapping point, and the valley value appeared at 0.08 L. When the inner wall temperature of the nozzle flowmeter was 50 °C, 100 °C, 300 °C, 500 °C and 700 °C, the maximum peak values of the monitoring path 1 were 0.00049 W/mm², 0.0013 W/mm², 0.0046 W/mm², 0.0079 W/mm² and 0.011 W/mm², respectively. It showed that as the temperature of the inner wall of the nozzle flowmeter increased, the Y-direction heat flow peak value of the monitoring path 1 also increased.

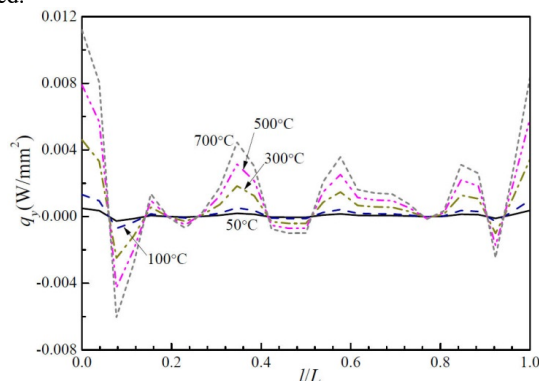


Fig. 9 Heat flow distribution of monitoring path 1 in Y direction at different inner wall temperatures

When the inner wall temperature of the nozzle flowmeter was 50 °C, 100 °C, 300 °C, 500 °C and 700 °C, the minimum valley values of monitoring path 1 were -0.00027 W/mm², -0.00071 W/mm², -0.0025 W/mm², -0.0043 W/mm² and -0.00604 W/mm², respectively. When the inner wall temperature of nozzle flowmeter was 50 °C, 100 °C, 300 °C, 500 °C and 700 °C, the maximum amplitudes (maximum peak - minimum valley) of monitoring path 1 were 0.00076 W/mm², 0.00201 W/mm², 0.0071 W/mm², 0.0122 W/mm² and 0.017 W/mm², respectively. It showed that as the inner wall temperature of the nozzle flowmeter increased, the maximum amplitude of the Y-direction heat flow on the monitoring path 1 also increased.

Fig. 10 shows the heat flow distribution of monitoring path 2 in Y direction at different inner wall temperatures. In all cases, the heat flow peak in the Y direction appeared at 0.19 L on the path from the inner wall to the outer wall. When the inner wall temperature of the nozzle flowmeter was 50 °C, 100 °C, 300 °C, 500 °C and 700 °C, the

maximum peak values of the Y-direction heat flux on the monitoring path 2 were 0.00305 W/mm², 0.00813 W/mm², 0.02847 W/mm², 0.0488 W/mm² and 0.069 W/mm², respectively. It showed that as the inner wall temperature of the nozzle flowmeter increased, the Y-direction heat flow peak of the monitoring path 2 also increased.

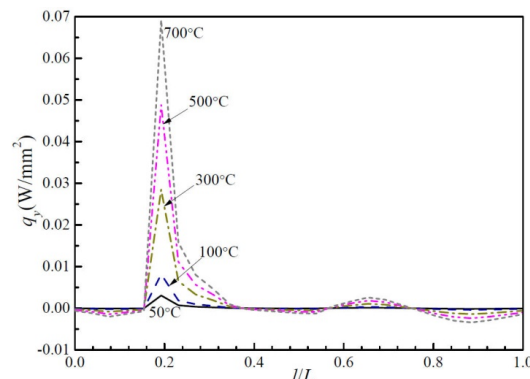


Fig. 10 Heat flow distribution of monitoring path 2 in Y direction at different inner wall temperatures

Fig. 11 shows the heat flow distribution of monitoring path 1 in Z direction at different inner wall temperatures. In all cases, the heat flow in the Z direction increased first, then decreased and then increased on the path from the upstream pressure tapping point to the downstream pressure tapping point. The peak values appeared at 0.42 L and 0.58 L, and valley value appeared at 0.5 L. When the inner wall temperature of the nozzle flowmeter was 50 °C, 100 °C, 300 °C, 500 °C and 700 °C, the maximum peaks of the monitoring path 1 were 0.037325 W/mm², 0.099535 W/mm², 0.34837 W/mm², 0.59721 W/mm² and 0.84604 W/mm², respectively.

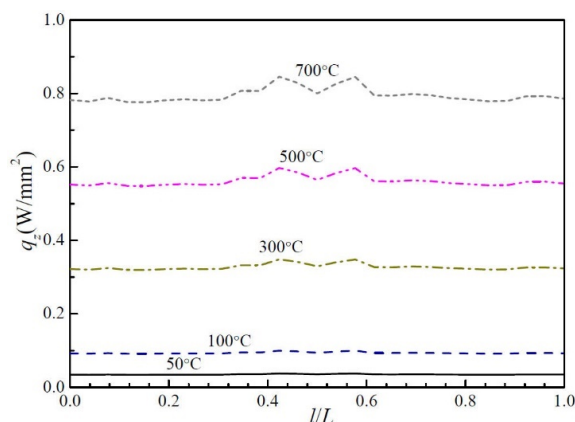


Fig. 11 Heat flow distribution of monitoring path 1 in Z direction at different inner wall temperatures

It showed that as the inner wall temperature of the nozzle flowmeter increased, the Z-direction heat flow peak value of the monitoring path 1 also increased. When the inner wall temperature of the nozzle flowmeter was 50 °C, 100 °C, 300 °C, 500 °C and 700 °C, the Z-direction heat flow values at 0.5 L of the monitoring path 1 were 0.035299 W/mm², 0.094131 W/mm², 0.32946 W/mm², 0.56479 W/mm² and 0.80011 W/mm², respectively. When the inner wall temperature of nozzle flowmeter was 50 °C, 100 °C, 300 °C, 500 °C and 700 °C, the maximum amplitude (maximum peak - minimum valley) of monitoring path 1 were 0.002807 W/mm², 0.007488 W/mm², 0.0262 W/mm², 0.04493 W/mm² and 0.06364 W/mm², respectively. It showed that as the inner wall temperature of the nozzle flowmeter increased, the maximum amplitude of the Z-direction heat flow on the monitoring path 1 also increased. It can be seen that the total heat flow field of monitoring path 1 at different inner wall temperatures was mainly determined by the Z-direction heat flow field.

Fig. 12 shows the heat flow distribution of monitoring path 2 in Z direction under different inner wall temperatures. In all cases, the heat flow in Z direction increased at first and then decreased in the path from inner wall to outer wall, and reached the peak at 0.35 L. When the inner wall temperature of the nozzle flowmeter was 50 °C, 100 °C, 300 °C, 500 °C and 700 °C, the maximum peaks of the Z-direction heat flux on the monitoring path 2 were 0.036351 W/mm², 0.096936 W/mm², 0.33928 W/mm², 0.58162 W/mm² and 0.82396 W/mm², respectively. It showed that as the inner wall temperature of the nozzle flowmeter increased, the Z-direction heat flow peak value of the monitoring path 2 also increased. When the inner wall temperature of nozzle flowmeter was 50 °C, 100 °C, 300 °C, 500 °C and 700 °C, the maximum amplitude (maximum peak - minimum valley) of monitoring path 1 were 0.0327101 W/mm², 0.087227 W/mm², 0.305299 W/mm², 0.523366 W/mm² and 0.741434 W/mm². It showed that the maximum amplitude of the monitoring path 2 increased as the inner wall temperature of the nozzle flowmeter increased. It can be seen that the total heat flow field of monitoring path 2 at different inner wall temperatures was mainly determined by the Z-direction heat flow field.

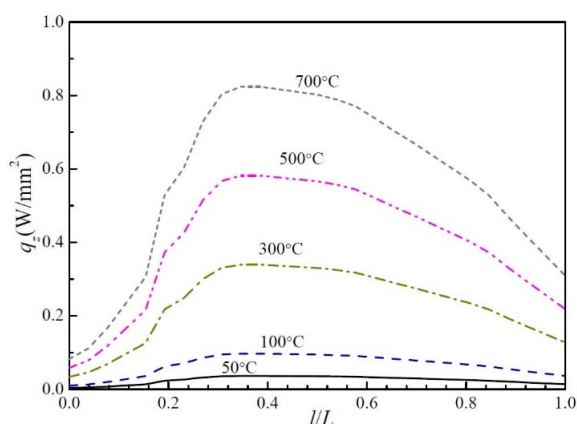


Fig. 12 Heat flow distribution of monitoring path 2 in Z direction under different inner wall temperatures

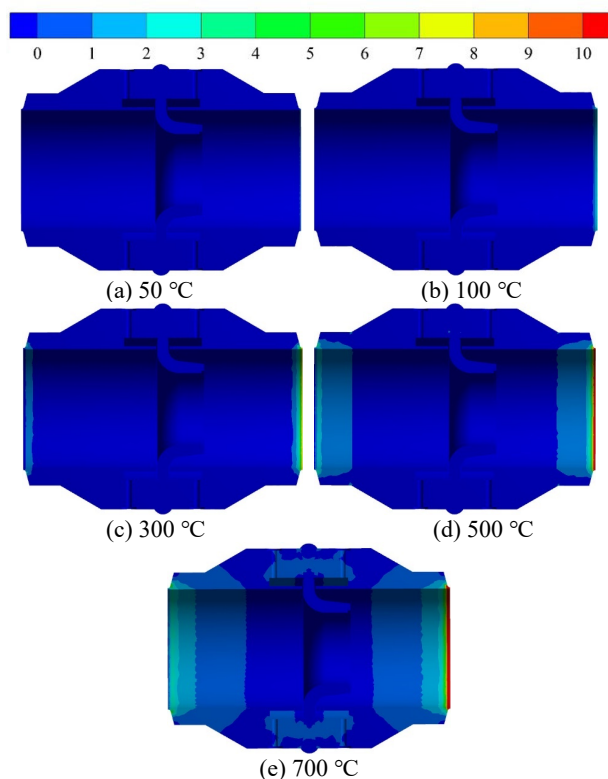


Fig. 13 Total heat flow distributions under different inner wall temperatures

Fig. 13 shows the total heat flow distributions under different inner wall temperatures. When the outer wall temperature was constant at 20 °C, the total heat flow distribution inside the nozzle flowmeter gradually expanded to the inlet and outlet with the increase of the inner wall temperature. When the inner wall temperature rose from 50 °C to 700 °C, the heat flow field at the inlet and outlet of the flowmeter increased significantly with the increase of temperature. When the inner wall temperature of the nozzle flowmeter was 700 °C, an obvious heat flow area appeared at the upstream pressure tapping point, downstream pressure tapping point, the inlet and outlet of the nozzle flowmeter. The maximum heat flow value of 10 W/mm² appeared at the outlet of the nozzle flowmeter. When the inner wall temperature of the nozzle flowmeter was 50 °C, the internal heat was weak, and the heat flow value ranged from 0 to 1 W/mm². It showed that the higher the inner wall temperature of the nozzle flowmeter was, the more frequent the internal heat transfer and heat exchange were.

3.3 Transient temperature field analysis

Fig. 14 shows the transient temperature distribution of the flowmeter when the inner wall temperature is 50 °C. When the outer wall temperature was constant at 20 °C and the inner wall was 50 °C, due to heat transfer effect, the heat on the inner wall of flowmeter gradually transferred to the outer wall, and the heat on the outer wall of the eight-slot nozzle gradually transferred to the internal central region. At t = 0 s, there was an area inside the flowmeter with low temperature, which was 12 °C. At t = 1.5 s, the heat of the inner wall gradually transferred to the outer wall, and the lower temperature area inside gradually disappeared. During t = 3.0~7.5 s, the temperature around the upstream and downstream pressure tapping points and inside the eight-slot nozzle gradually increased. At t = 7.5 s, the temperature inside the eight-slot nozzle increased to 50 °C. It can be seen that with the passage of time, the heat on the inner wall of flow meter will transfer to the outer wall.

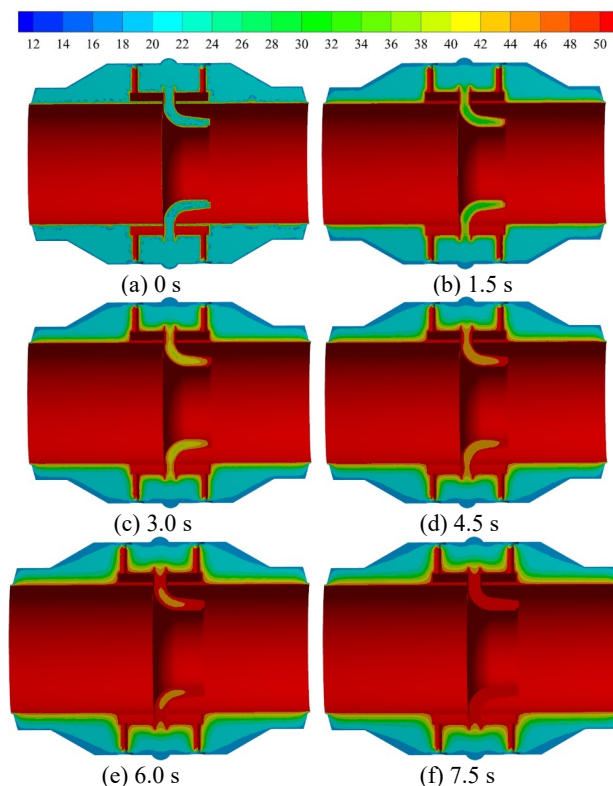


Fig. 14 Transient temperature distribution of the flowmeter when the inner wall temperature is 50 °C

Fig. 15 shows the transient temperature distribution of the flowmeter when the inner wall temperature is 100 °C. When the outer wall temperature was constant at 20 °C and the inner wall was 100 °C, due to heat transfer effect, the heat on the inner wall of flowmeter gradually transferred to the outer wall, and the heat on the outer wall of the eight-slot nozzle gradually transferred to the internal central region. At $t = 0$ s, there was an area inside the flowmeter with low temperature, which was 10 °C. At $t = 3.0$ s, the heat of the inner wall gradually transferred to the outer wall, and the lower temperature area inside gradually disappeared. During $t = 4.5\text{--}7.5$ s, the temperature around the upstream and downstream pressure tapping points and inside the eight-slot nozzle gradually increased. However, due to the slow rate of heat transfer, an obvious temperature stratification occurred near the inner wall, and the area where the temperature was between 30 °C and 40 °C was the largest part. At $t = 7.5$ s, the temperature inside the eight-slot nozzle increased to 70 °C.

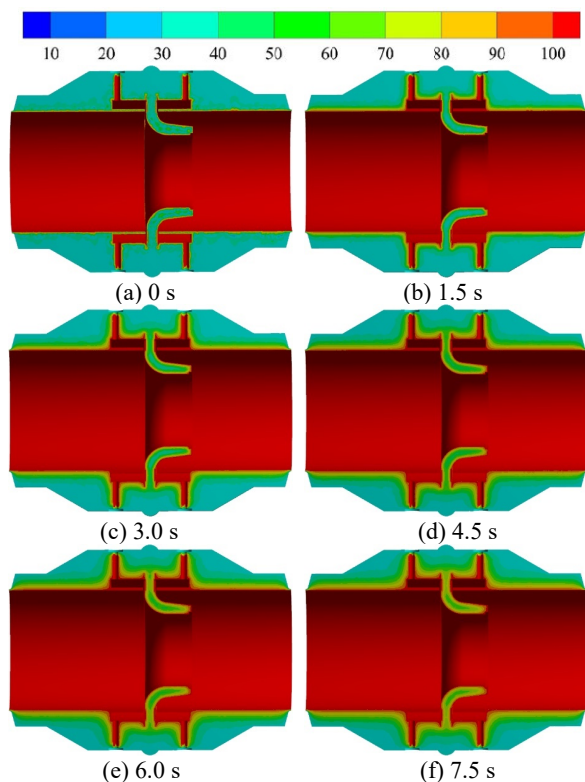


Fig. 15 Transient temperature distribution of the flowmeter when the inner wall temperature is 100 °C

Fig. 16 shows the transient temperature distribution of the flowmeter when the inner wall temperature is 300 °C. When the outer wall temperature was constant at 20 °C and the inner wall was 300 °C, due to heat transfer effect, the heat on the inner wall of flowmeter gradually transferred to the outer wall, and the heat on the outer wall of the eight-slot nozzle gradually transferred to the internal central region. At $t = 0$ s, there was an area inside the flowmeter with low temperature, which was 10 °C. At $t = 3.0$ s, the heat of the inner wall gradually transferred to the outer wall, and the lower temperature area inside gradually disappeared. During $t = 4.5\text{--}7.5$ s, the temperature around the upstream and downstream pressure tapping points and inside the eight-slot nozzle gradually increased. However, due to the slow rate of heat transfer, an obvious temperature stratification occurred near the inner wall, and the area where the temperature was between 68 °C and 97 °C was the largest part. At $t = 7.5$ s, the temperature inside the eight-slot nozzle increased to 184 °C.

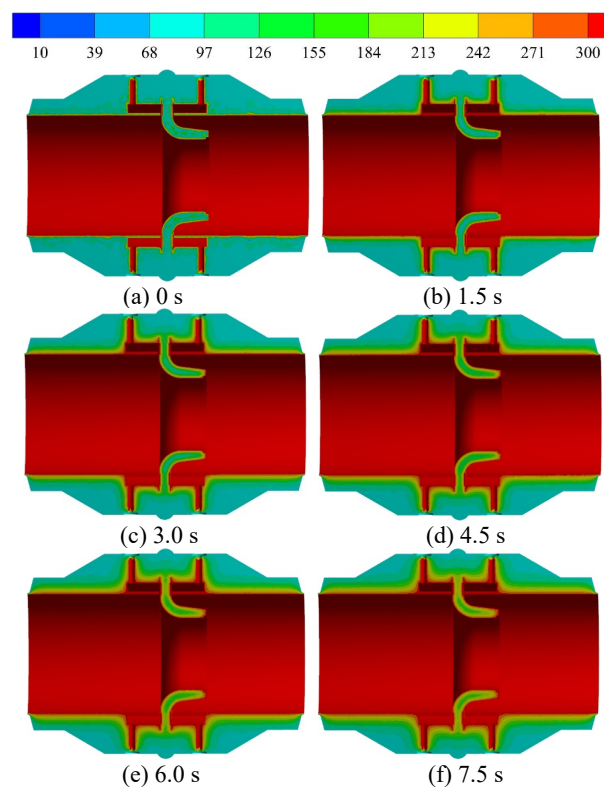


Fig. 16 Transient temperature distribution of the flowmeter when the inner wall temperature is 300 °C

Fig. 17 shows the transient temperature distribution of the flowmeter when the inner wall temperature is 500 °C. When the outer wall temperature was constant at 20 °C and the inner wall was 500 °C, due to heat transfer effect, the heat on the inner wall of flowmeter gradually transferred to the outer wall, and the heat on the outer wall of the eight-slot nozzle gradually transferred to the internal central region.

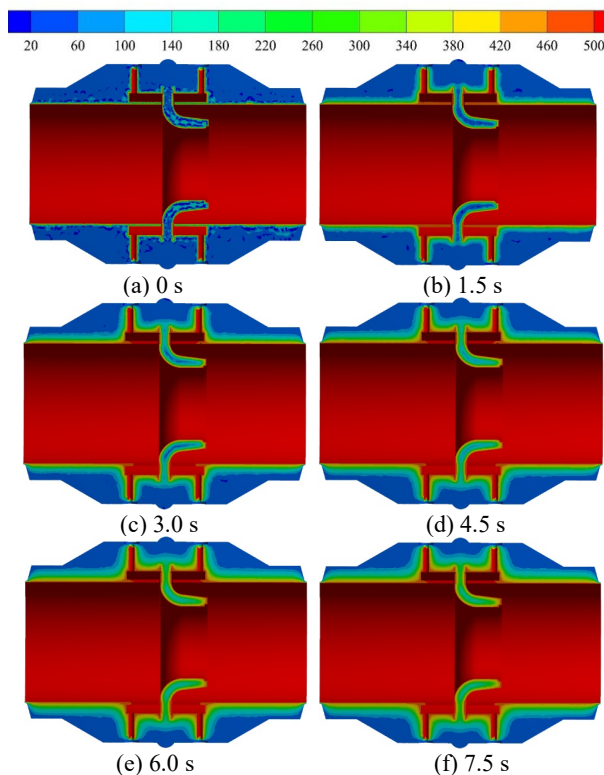


Fig. 17 Transient temperature distribution of the flowmeter when the inner wall temperature is 500 °C

At $t = 0$ s, there was an area inside the flowmeter with low temperature, which was $20\text{ }^{\circ}\text{C}$. At $t = 3.0$ s, the heat of the inner wall gradually transferred to the outer wall, and the lower temperature area inside gradually disappeared. During $t = 4.5\sim 7.5$ s, the temperature around the upstream and downstream pressure tapping points and inside the eight-slot nozzle gradually increased. However, due to the slow rate of heat transfer, an obvious temperature stratification occurred near the inner wall. The area where the temperature was between $60\sim 100\text{ }^{\circ}\text{C}$ (near the outer wall) was the largest part. The area of the high temperature zone near the inner wall significantly increased. At $t = 7.5$ s, the temperature inside the eight-slot nozzle increased to $300\text{ }^{\circ}\text{C}$.

Fig. 18 shows the transient temperature distribution of the flowmeter when the inner wall temperature is $700\text{ }^{\circ}\text{C}$. When the outer wall temperature was constant at $20\text{ }^{\circ}\text{C}$ and the inner wall was $700\text{ }^{\circ}\text{C}$, due to heat transfer effect, the heat on the inner wall of flowmeter gradually transferred to the outer wall, and the heat on the outer wall of the eight-slot nozzle gradually transferred to the internal central region. At $t = 0$ s, there was an area inside the flowmeter with low temperature, which was $20\text{ }^{\circ}\text{C}$. At $t = 3.0$ s, the heat of the inner wall gradually transferred to the outer wall, and the lower temperature area inside gradually disappeared. During $t = 4.5\sim 7.5$ s, the temperature around the upstream and downstream pressure tapping points and inside the eight-slot nozzle gradually increased. However, due to the slow rate of heat transfer, an obvious temperature stratification occurred near the inner wall. The area where the temperature was between $100\sim 140\text{ }^{\circ}\text{C}$ (near the outer wall) was the largest part. The area of the high temperature zone near the inner wall significantly increased. At $t = 7.5$ s, the temperature inside the eight-slot nozzle increased to $460\text{ }^{\circ}\text{C}$.

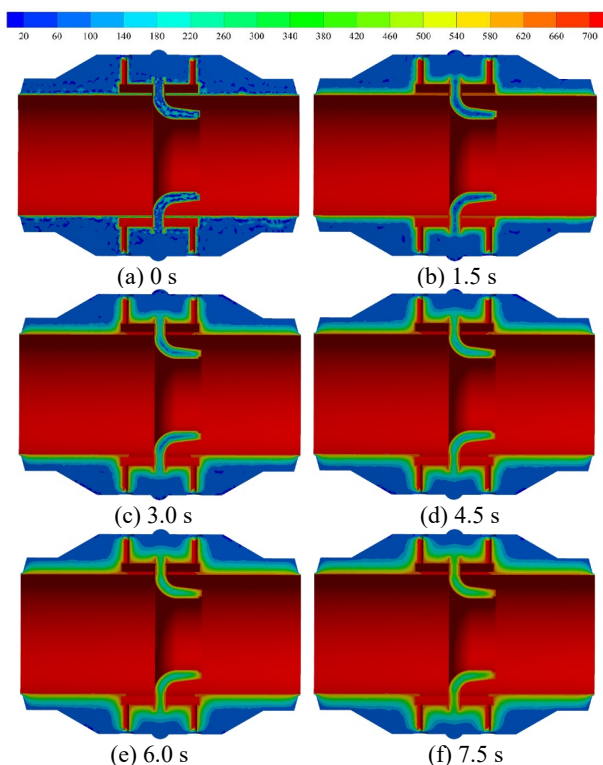


Fig. 18 Transient temperature distribution of the flowmeter when the inner wall temperature is $700\text{ }^{\circ}\text{C}$

4 CONCLUSION

A numerical model of a small nozzle flowmeter was developed and the simulation results showed that the numerical calculation method can effectively reveal the internal thermal characteristics:

(1) Under different inner wall temperatures, on the path from the upstream pressure tapping point to the downstream pressure tapping

point, there were multiple peaks and valleys on the heat flow distribution in the Y direction, and the valley values were all reached at 0.08 L .

(2) Under different inner wall temperatures, on the path from the upstream pressure tapping point to the downstream pressure tapping point, there appeared the same decreasing-increasing-decreasing trend on the heat flow distribution in the X direction, and the valley value and peak value were reached at 0.35 L and 0.73 L , respectively.

(3) Under different inner wall temperatures, on the path from the upstream pressure tapping point to the downstream pressure tapping point, there appeared the same increasing-decreasing-increasing trend on the heat flow distribution in the Z direction, and the peak values were reached at 0.42 L and 0.58 L and valley value at 0.5 L .

(4) When the inner wall temperature rose from $50\text{ }^{\circ}\text{C}$ to $700\text{ }^{\circ}\text{C}$, the heat flows at the inlet and outlet of the flowmeter increased significantly with the increase of temperature.

ACKNOWLEDGEMENTS

The research was financially supported by the "Pioneer" and "Leading Goose" R&D Program of Zhejiang (Grant No. 2022C03170) and Science and Technology Project of Quzhou (Grant No.2022K98).

REFERENCES

- Bilicki, Z., Giot, M., and Kwizdzinski, R., 2002, "Fundamentals of two-phase flow by the method of irreversible thermodynamics," *International journal of multiphase flow*, **28**(12), 1983-2005.
[https://doi.org/10.1016/S0301-9322\(02\)00107-6](https://doi.org/10.1016/S0301-9322(02)00107-6)
- Chen, D.S., Cui, B.L., and Zhu, Z.C., 2016, "Internal Flow Characteristics and Aft-cone Angle on Performance of Swirlmeter," *MĀPAN : journal of Metrology Society of India*, **31**(2), 107–113.
<https://doi.org/10.1007/s12647-015-0162-0>
- Cheng, H.Y., Bai, X.R., Long, X.P., Ji, B., Peng, X.X. and Farhat, M., 2020, "Large eddy simulation of the tip-leakage cavitating flow with an insight on how cavitation influences vorticity and turbulence," *Applied Mathematical Modelling*, **77**, 788-809.
<https://doi.org/10.1016/j.apm.2019.08.005>
- Cheng, L., Zhang, Y.L., and Li, J.F., 2022, "Diagnosis of Centrifugal Pump Speed Fluctuation by Using Vortex Dynamics," *Frontiers in Heat and Mass Transfer*, **19**, 32.1-7.
<http://dx.doi.org/10.5098/hmt.19.32>
- Cheng, L., and Zhang, Y.L., 2022, "Self-coupling numerical calculation of centrifugal pump startup process," *Frontiers in Heat and Mass Transfer*, **18**, 26.1-6.
<http://dx.doi.org/10.5098/hmt.18.26>
- Cui, B.L., Lu, Z.Q., Chen, D.S., Chen, K., and Huang, D.H., 2015, "Influence of incident angle of swirler on performance of swirl meter," *Transactions of the Chinese Society of Agricultural Engineering*, **31**(2), 53-58.
<https://doi.org/10.3969/j.issn.1002-6819.2015.02.008>
- Cui, B.L., Zhang, C.L., and Zhang, Y.L., 2020, "Experimental and numerical studies on metrological characteristics of swirlmeters with different swirler helix angles in a gas–solid two-phase flow," *Flow measurement and instrumentation*, **74**, 101779.1-17.
<https://doi.org/10.1016/j.flowmeasinst.2020.101779>
- DeOtte, R.E., Morrison, G.L., Panak, D.L., and Nail, G.H., 1991, "3-D laser Doppler anemometry measurements of the axisymmetric flow field near an orifice plate," *Flow Measurement and Instrumentation*, **2**(2), 115-123.
[http://dx.doi.org/10.1016/0955-5986\(91\)90019-N](http://dx.doi.org/10.1016/0955-5986(91)90019-N)

- Fu, X., and Yang H.Y., 2001, "Study on mechanism of hydrodynamic oscillation in vortex precession meter using large eddy simulation," *Chinese Journal of Mechanical Engineering*, **14**(1), 9-11.
<http://dx.doi.org/10.3901/cjme.2001.01.009>
- He, X.Y., Su, Z.D., Yin, X.J., and Zhou, K., 2008, "A numerical study on the flow characteristics in swirlmeter," *Journal of China Jiliang University*, **19**(4), 134–137. (in Chinese with English abstract)
<http://dx.doi.org/10.3969/j.issn.1004-1540.2008.04.005>
- Huang, S.F., Ma, T.Y., Wang, D., and Lin, Z.H., 2013, "Study on discharge coefficient of perforated orifices as a new kind of flowmeter," *Experimental Thermal and Fluid Science*, **46**, 74-83.
<http://dx.doi.org/10.1016/j.expthermflusci.2012.11.022>
- Jia, X.Q., Hao, L., and Zu C.Z., 2022, "Unsteady flow characteristics of an AFP based on energy loss and vortex identification under rotating stall condition," *Journal of Process Mechanical Engineering*, Online.
<http://dx.doi.org/10.1177/09544089221136685>
- Jia, X.Q., Lv, H., and Zhu Z.C., 2023, "Research on the Influence of Impeller Tip Clearance on the Internal Flow Loss of Axial Circulating Pump Under Unpowered Driven Condition," *Journal of Fluids Engineering*, **145**(2): 021202.1-12.
<http://dx.doi.org/10.1177/09544089221136685>
- Jia, X.Q., Zhang, Y., Lv, H., and Zhu, Z.C., 2023, "Study on external performance and internal flow characteristics in a centrifugal pump under different degrees of cavitation," *Physics of Fluids*, **35**(1), 1-15.
<http://dx.doi.org/10.1063/5.0133377>
- Jin, X.M., 2014, "Analysis of the advantages vortex precession flowmeter measurement," *Instrument Analysis Monitoring*, **2**, 36-39.
<http://dx.doi.org/10.3969/j.issn.1002-3720.2014.02.011>
- Kim, B.C., Pak, B.C., Cho, N.H., Chi, D.S. Choi, H.M. Choi, Y.M., and Park, K.A., 1998, "Effects of cavitation and plate thickness on small diameter ratio orifice meters," *Flow Measurement and Instrumentation*, **8**(2), 85-92.
[http://dx.doi.org/10.1016/S0955-5986\(97\)00034-4](http://dx.doi.org/10.1016/S0955-5986(97)00034-4)
- Kock, F., and Herwig, H., 2004, "Local entropy production in turbulent shear flows: a high-Reynolds number model with wall functions," *International journal of heat and mass transfer*, **47**(10), 2205-2215.
<https://doi.org/10.1016/j.ijheatmasstransfer.2003.11.025>
- Kolodzie Jr, P.A., and Van Winkle, M., 1957, "Discharge coefficients through perforated plates," *American Institute of Chemical Engineers*, **3**(3), 305-312
<http://dx.doi.org/10.1002/aic.690030304>
- Li, H.Z., Liang, Q.C., and Cui, H.G., 2012, "Research on the meter coefficient and simulation analysis of a new swirlmeter," *Applied Mechanics and Materials*, **127**, 421-427.
<http://dx.doi.org/10.4028/www.scientific.net/AMM.127.421>
- Ma, C.W., and Zhao, X.H., 2014, "An experimental research on anti-vibration of swirlmeter based on difference method," *Journal of Tianjin University of Technology*, **5**, 6-9. (in Chinese with English abstract)
<http://dx.doi.org/10.3969/j.issn.1673-095X.2014.05.002>
- Morrison, G.L., Deotte Jr, R.E., Nail, G.H., and Panak, D.L., 1993, "Mean velocity and turbulence fields inside a $\beta=0.50$ orifice flowmeter," *American Institute of Chemical Engineers*, **39**(5), 745-756.
<http://dx.doi.org/10.1002/aic.690390503>
- Numachi, F., Yamabe, M., and Ōba, R., 1960, "Cavitation Effect on the Discharge Coefficient of the Sharp-Edged Orifice Plate," *Journal of Fluids Engineering*, **82**(1), 1-6.
<http://dx.doi.org/10.1115/1.3662523>
- Peng J.G., Fu X., and Chen, Y., 2004, "A method for removal of fluid pulsating interference on swirlmeter based on spectrum phase discrimination using FFT," *Chinese Journal of Scientific Instrument*, **25**(2), 217-221. (in Chinese with English abstract)
<http://dx.doi.org/10.3321/j.issn:0254-3087.2004.02.020>
- Pirouzpanah, S., Çevik, M., and Morrison, G.L., 2014, "Multiphase flow measurement using coupled slotted orifice plate and swirl flow meter," *Flow Measurement and Instrumentation*, **40**, 157-161.
<http://dx.doi.org/10.1016/j.flowmeasinst.2014.09.005>
- Schena, E., Cecchini, S., and Silvestri, S., 2013, "An orifice meter for bidirectional air flow measurements: Influence of gas thermo-hygrometric content on static response and bidirectionality," *Flow Measurement and Instrumentation*, **34**, 105-112.
<http://dx.doi.org/10.1016/j.flowmeasinst.2013.09.001>
- Smith Jr, P.L., and Van Winkle, M., 1958, "Discharge coefficients through perforated plates at Reynolds numbers of 400 to 3,000," *American Institute of Chemical Engineers*, **4**(3), 266-268.
<http://dx.doi.org/10.1002/aic.690040306>
- Tao, J.Y., Lin, Z., Ma, C.J., Ye, J.H., Zhu, Z.C., Li, Y., and Mao, W., 2020, "An experimental and numerical study of regulating performance and flow loss in a v-port ball valve," *Journal of fluids engineering*, **142**(2), 1-9
<https://doi.org/10.1115/1.4044986>
- Zhang, C.L., Cui, B.L., Zhang, Y.L., Zhu, Z.C., and Sheng, Y.N., 2019, "Experimental and numerical study on swirlmeter with different helix angles of swirler," *Transactions of the Institute of Measurement and Control*, **41**(11), 3103-3120.
<https://doi.org/10.1177/0142331218823859>